Korean J. Chem. Eng., 37(9), 1589-1598 (2020)
DOI: 10.1007/s11814-020-0531-4

pISSN: 0256-1115
eISSN: 1975-7220

Multi-functional NiO/g-C_3N_4 hybrid nanostructures for energy storage and sensor applications

Yen-Linh Thi Ngo, Jin Suk Chung†, and Seung Hyun Hur†

School of Chemical Engineering, University of Ulsan, Daehak-ro 93, Nam-gu, Ulsan 44610, Korea
(*Received 30 December 2019 • Revised 19 January 2020 • Accepted 28 February 2020*)

Abstract−A multi-functional NiO/g-C_3N_4 (NC) hybrid nanostructure was synthesized by a hydrothermal process using melamine and $Ni(OH)_2$ as precursors followed by thermal treatment. The optimal conditions were determined by studying the process conditions, such as the $Ni(OH)_2$ to melamine ratio and thermal treatment temperature. The NC prepared in this study exhibited both excellent glucose sensing properties and supercapacitor properties. A very high glucose sensitivity, as high as 5,387.1 μA $mM^{-1}cm^{-2}$, and excellent energy density of 49.6 Wh kg^{-1} at a power density of 1,064.2 W kg^{-1} were obtained when NC was used as the electrode material for glucose sensing and symmetric supercapacitor, respectively. A flexible glucose sensing device using a flexible substrate and self-powered glucose sensor system that used the same material (NC) for the both power supply and sensing devices were also demonstrated.

Keywords: Graphitic Carbon Nitride, Nickel Oxide, Glucose Sensor, Non-enzymatic Sensor, Supercapacitor

INTRODUCTION

Diabetes, a disease caused by endocrine disorder of the carbohydrate metabolism, is one of the major health problems that affects the life of millions of people around the world [1-3]. Therefore, the development of a reliable, sensitive, and selective method for monitoring glucose is essential for controlling the glucose level in many areas, including biological medicine, food industry, and clinical diagnoses. Since Clark and Lyons proposed the first enzyme-based electrode in 1962 [4], many studies using glucose oxidase (GOx) have been developed because of their excellent sensitivity and selectivity. On the other hand, enzymatic sensors still have several drawbacks, including a lack of stability, strict operating conditions, and high-cost due to the intrinsic nature of biomaterials [5,6]. To overcome such problems, non-enzymatic glucose sensors have been explored extensively to determine the glucose concentration without using enzymes. This will allow the direct electrocatalytic oxidation of glucose on a metal or inorganic catalyst electrode surface. Recent studies have shown that the slow response time, low sensitivity, poor selectivity, and less stability caused by intermediate-induced surface poisoning are the most important issues to be solved before non-enzymatic sensors can be used in real applications [2].

The working mechanism of the non-enzymatic glucose sensor is related to the electrocatalytic oxidation of glucose to gluconolactone in the presence of an electrocatalyst. In this regard, nanomaterials with high electrocatalytic ability towards glucose oxidation, including metal and their oxide (Ag [7], Au [8], Pt [9], NiO [10], CuO [11], Co_3O_4 [12]), or composite materials [13,14], have been studied widely as an electrode material for non-enzymatic glucose sensors. Among them, NiO has attracted considerable interest as an electrode material in electrochemical reactions because of its good stability, low cost, and high catalytic activity towards the glucose oxidation reaction [15,16]. Thus far, different morphologies of NiO have been demonstrated using a range of preparation methods, and their morphology-dependent properties have also been widely studied [17-19]. On the other hand, the low conductivity and sensitivity of the pristine NiO electrode should be solved before NiO can be used as an electrode material for glucose detection. In this regard, a hybrid of NiO with highly conductive materials can lead to improved electrical and electrochemical properties [18,20].

Recently, graphitic carbon nitride (g-C_3N_4), a type of 2D material, has become a potential candidate in a range of applications, such as biosensors [21,22], energy storage [23-25], catalysts [26,27], photocatalysts [28], water splitting materials [29], and oxygen reduction reaction materials [30], because of its unique optical properties, thermal/chemical stability, and inexpensive synthesis process. In addition, g-C_3N_4 exhibits excellent electrical conductivity and effective charge transfer with other materials because of the high π-conjugation of the sp^2-hybridized N-substituted graphite framework [31]. Therefore, the hybridization of nanomaterials with g-C_3N_4 can enhance their original properties for a range of applications, particularly in electrochemical sensors and energy storage.

Previous studies have shown that the hybridization of electrocatalysts, such as $NiMn_2O_4$ [14] or Co_3O_4 [12] with conductive reduced graphene oxide, can strongly improve their electrocatalytic activity. In this study, the NiO/g-C_3N_4 hybrid structure (NC) was prepared using a controlled thermal treatment under a nitrogen atmosphere. The structure was then employed as an electrode material for non-enzymatic glucose sensors and symmetric supercapacitors. The electrochemical properties of NC were examined by cyclic voltammetry. The NC exhibited extremely high glucose sensitivity, up to 5,387.1 μA $mM^{-1}cm^{-2}$, which is one of the highest values ever reported. This also shows a low detection limit, excellent selectivity, good long-term stability, and rapid response towards glucose. When monitor-

†To whom correspondence should be addressed.
E-mail: shhur@ulsan.ac.kr, jschung@ulsan.ac.kr

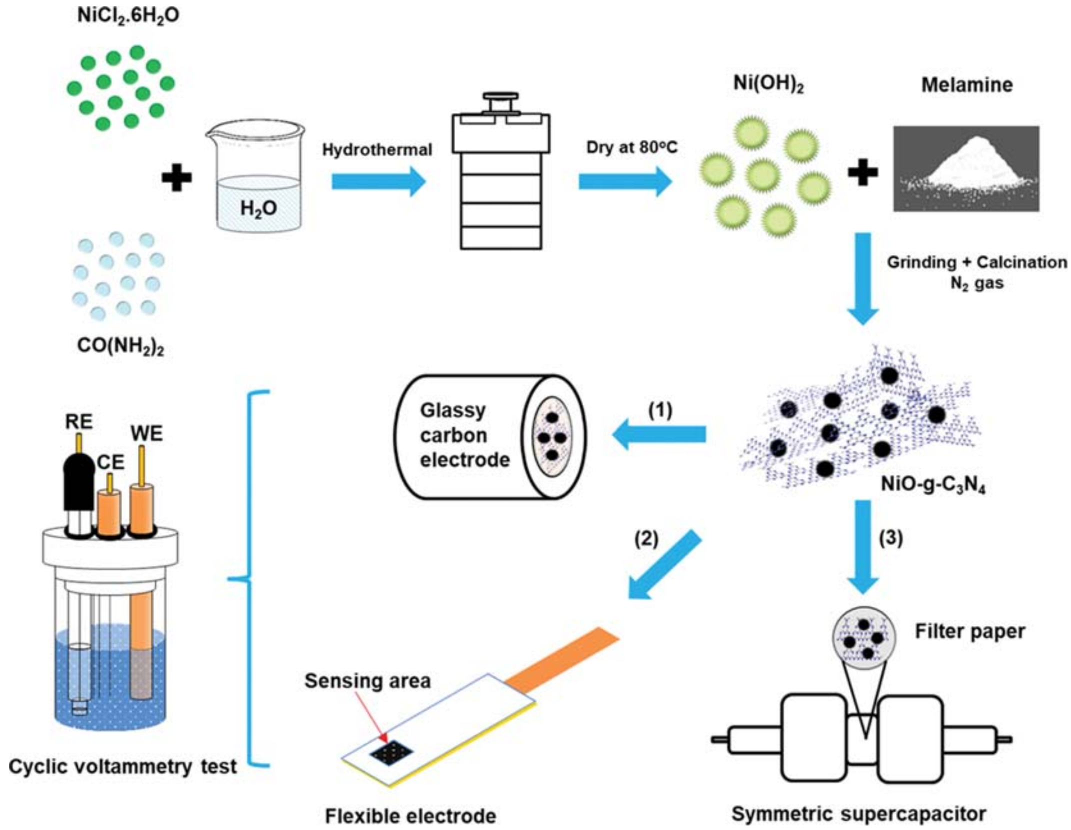

Scheme 1. Schematic diagram of the preparation process of NiO/g-C_3N_4 hybrid materials (NC) and NC based electrodes.

ing the glucose level in real blood serum, the results were comparable to the enzyme-based commercial glucose sensor. A flexible glucose sensor was also fabricated using NC as an electrode material, which could maintain its sensitivity even after more than 100 severe bending tests. In addition, the NC-based supercapacitor showed very high capacitance (357.10 F g^{-1} at a current density of 1 A g^{-1}) and excellent cycling stability and was then used effectively as the power source for NC-based glucose sensors.

EXPERIMENTAL DETAILS

Detailed information on the materials and instrumental analysis is described in the supporting information.

1. Synthesis of NiO/g-C_3N_4 Hybrid Materials

$Ni(OH)_2$ was fabricated using a facile hydrothermal treatment method. First, 2.5 g of $NiCl_2{\cdot}6H_2O$ and 1.0 g of $CO(NH_2)_2$ were dissolved in DI water under stirring until the solution became clear. The solution was then transferred to a Teflon-stainless steel autoclave and kept at 150 °C for 3 h. The green product was washed several times with DI and ethanol and dried overnight at 80 °C.

The NC was fabricated by $Ni(OH)_2$ and melamine. First, $Ni(OH)_2$ and melamine were mixed and ground by a mortar for 10 min. The mixture was treated thermally under a nitrogen environment (N_2) up to 370 °C with a ramping rate of 10 °C per min. The resulting products were ground again, washed with DI and ethanol, and dried at 80 °C. A range of hybrid materials were fabricated and labeled as NC(x), where x indicates the mass ratio of the precursor melamine and $Ni(OH)_2$. Scheme 1 shows the procedure for NC synthesis. The melamine and $Ni(OH)_2$ mixing ratio was confirmed by TGA (Fig. S1).

2. Preparation of the NiO/g-C_3N_4 Modified Electrodes

The NC was decorated on a glassy carbon electrode (GCE, 3 mm of diameter), which had been polished with alumina and diamond slurries and rinsed with DI water. A NC slurry was prepared by dispersing 1.0 mg of the sample in 50 μL Nafion in an isopropanol solution (5 wt%). Subsequently, a 10 μL solution was drop-coated on a GCE and dried at room temperature. The flexible NC/GCE working electrode was prepared except that the slurry of the NC composite was decorated onto the C ink/copper foil/transparent film (Fig. S12).

To fabricate symmetrical supercapacitor electrodes, 1.0 mg of sample was dispersed in 2 mL of 2 M KOH solution, and 1 mL of the suspension was drop cast on two microfiber filter papers with the thickness of 1 mm. Another microfiber filter paper was used as a separator between the two electrodes and 2 M KOH was used as the electrolyte.

RESULTS AND DISCUSSION

1. Characterization of Pristine g-C_3N_4, NiO, and NiO/g-C_3N_4

To investigate the functional groups, the FT-IR spectra of the NC(x) and pristine g-C_3N_4 were recorded, as shown in Fig. S2. The red dashed lines in the range of 1,150-1,630 cm^{-1} represent the typical stretching vibration of the C-N aromatic rings. The absorption peaks centered at 1,244, 1,322, and 1,408 cm^{-1} were assigned to the stretching vibration mode of C-N, C=N, and C=C in aromatic amine, respectively [32]. The peaks at 1,556 and 1,630 cm^{-1} correspond to the C=N stretching vibration modes of the tri-s-triazine structure. In addition, the characteristic out-of-plane bending vibration of the tri-s-triazine unit as the main peak was observed at 806 cm^{-1} for all samples, which demonstrates the presence of g-C_3N_4 [28]. As noted by the black-colored line, the peak at 460 cm^{-1} in all the NC(x) corresponds to the Ni-O stretching vibration [33], which confirms the successful fabrication NiO/g-C_3N_4 hybrid structures.

XRD was performed to determine the crystalline and phase structure of NC(x) after the thermal treatment, as shown in Fig. 1. The XRD pattern of g-C_3N_4 heat treated at 370 °C shows many XRD peaks that were similar to those of pristine melamine (Fig. S3A). On the other hand, the XRD pattern of g-C_3N_4 calcined at 550 °C shows a graphitic carbon nitride peak. The characteristic peaks shown in g-C_3N_4 calcined at 550 °C at 12.79° and 27.02° 2θ were assigned to the (100) and (002) planes of g-C_3N_4 (JCPDS Card No 87-1526), which represents the stacking of the motif and conjugated π-π systems in the aromatic unit of g-C_3N_4, respectively [28]. The XRD patterns of NC(x) exhibit sharper NiO peaks originating from the $Ni(OH)_2$ precursor (Fig. S3(b)), which confirms the high crystallinity of NiO after high temperature thermal treatment. The other peaks observed at 44.37° and 51.76° 2θ correspond to the

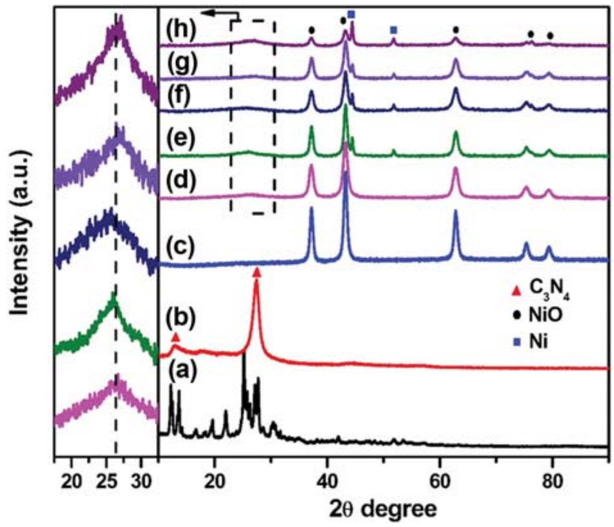

Fig. 1. XRD patterns of (a) g-C_3N_4 (calcined at 370 °C), (b) g-C_3N_4 (calcined at 550 °C), (c) NiO and (d)-(h) various NC(x) with x=0.5, 1, 2, 3, 4 corresponding to (d), (e), (f), (g) and (h), respectively.

(111) and (200) crystal plane of the Ni phase. Interestingly, the (002) plane can be observed clearly in NC(x), had been calcined at 370 °C, because of the catalytic effect of NiO, as observed by TGA (Fig. S1).

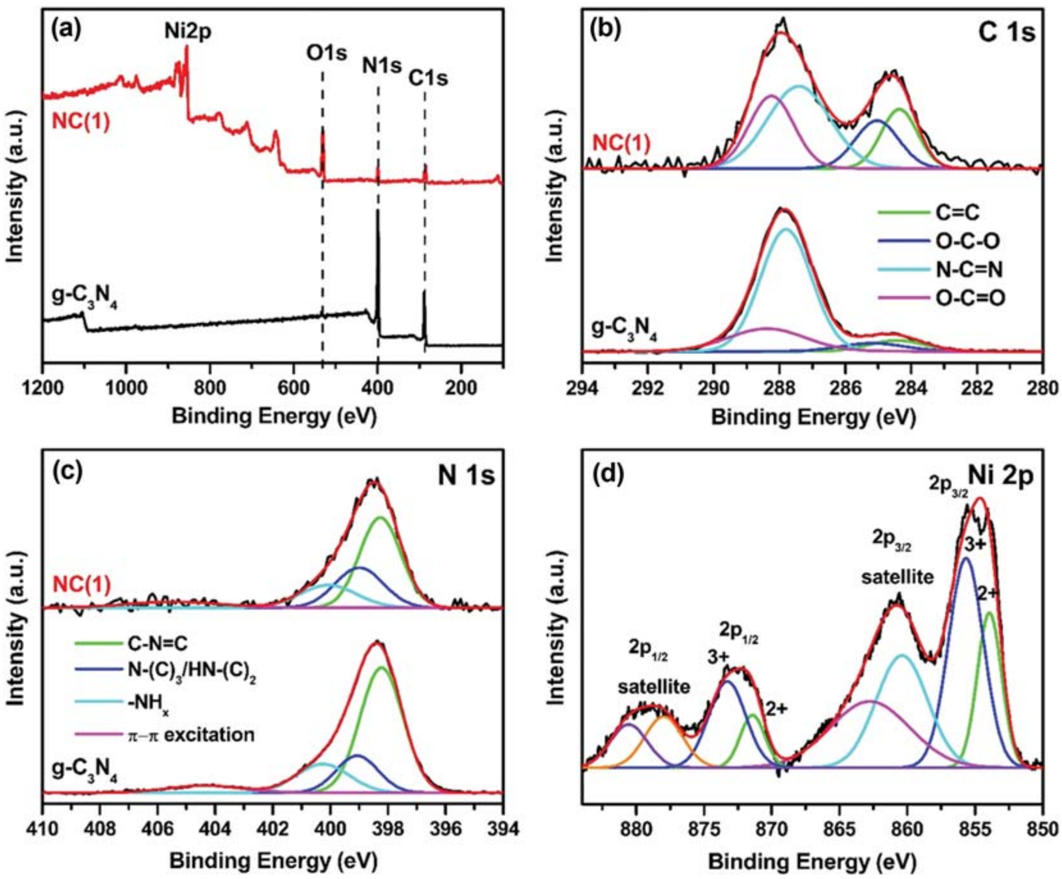

Fig. 2. (a) XPS survey and high-resolution (b) C 1s, (c) N 1s, and (d) Ni 2p XPS spectra of pristine g-C_3N_4 and NC(1) composite.

The oxidation state of carbon, nitrogen, and nickel in NC(1) and pure g-C_3N_4 was examined by XPS. Fig. 2 presents the XPS survey and high-resolution spectra of C 1s, N 1s, and Ni 2p of g-C_3N_4 and NC(1). As shown in Fig. 2(a), g-C_3N_4 is composed of only C, N, and O but NC(1) contains Ni. Deconvolution of the C 1s spectrum revealed four peaks centered at 284.5, 287.8, 285.2, and 288.4 eV, which were assigned to sp^2-hybridized carbon atoms (C=C), tertiary N-C=N coordination, and sp^3-hybridized carbon with oxygen groups (O-C-O and O-C=O/N-C=O) of the g-C_3N_4 structure, respectively (Fig. 2(b)) [34]. The high-resolution N 1s spectra (Fig. 2(c)) exhibit typical characteristic peaks at 398.3, 399.0, 400.2, and 404.6 eV, which correspond to sp^2-hybridized N (C-N=C), sp^3-hybridized N (N-$(C)_3$/HN-$(C)_2$), amino groups with hydrogen (N-H/NH_2 group), and π-π excitation charged of g-C_3N_4, respectively. The relative peak area ratio (Tables S1-S2) of C and N bonding obtained from the C 1s and N 1s spectra for the NC(1) is similar to those of g-C_3N_4, which indicates that there are no chemical changes in g-C_3N_4 after hybridization with NiO [23]. The Ni 2p core level spectrum of NC(1) (Fig. 2(d)) shows two major peaks at 854.7 and 872.8 eV, which were assigned to Ni $2p_{3/2}$ and Ni $2p_{1/2}$, respectively. The other peaks at 879.0 eV and 860.6 eV are satellite peaks of Ni $2p_{1/2}$ and Ni $2p_{3/2}$, respectively. The peaks at 853.9 and 871.4 eV after

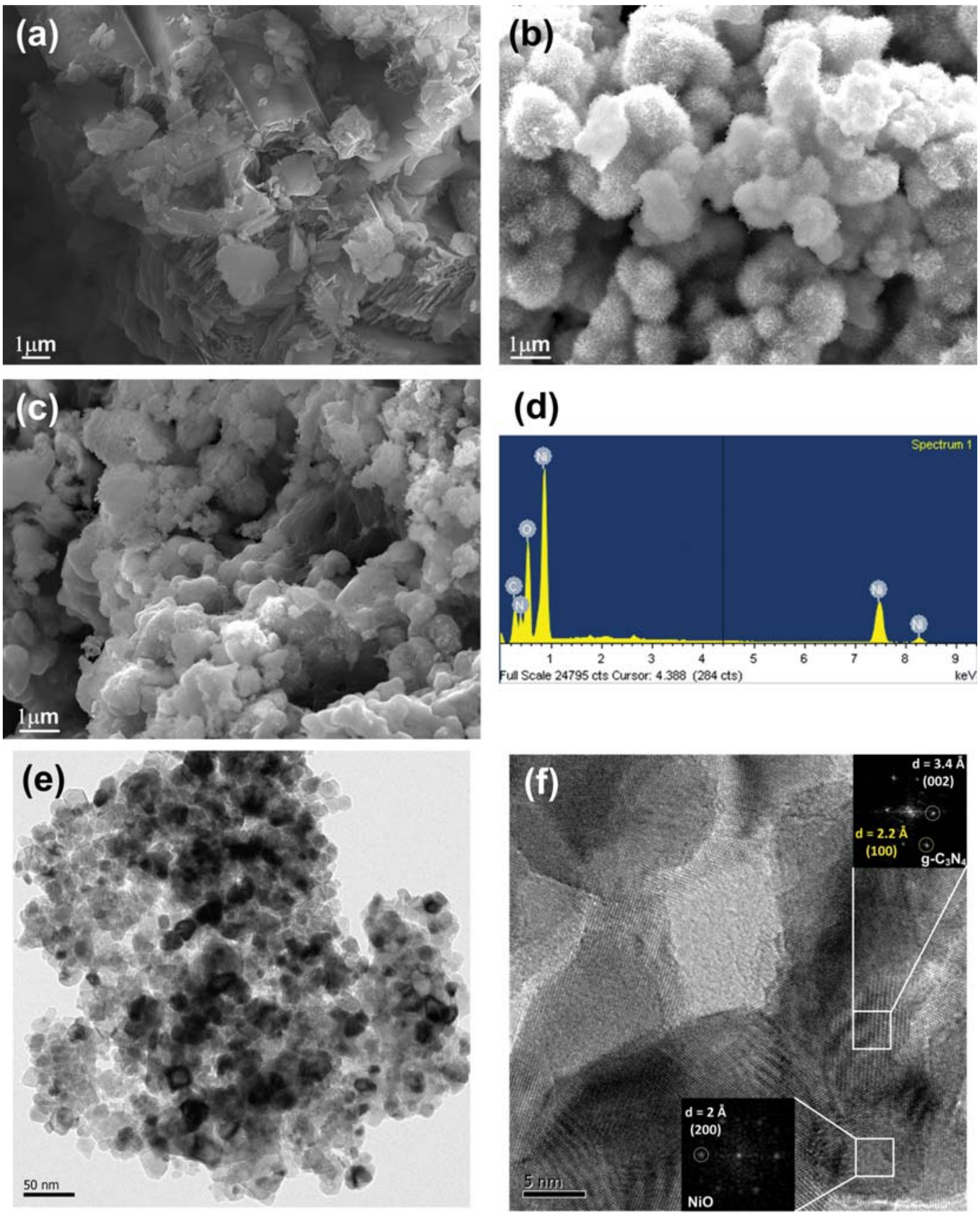

Fig. 3. FE-SEM images of (a) pristine g-C_3N_4 (calcined at 370 °C), (b) NiO and (c) NC(1). (d) EDS spectrum of NC(1). (e) TEM and (f) HR-TEM images of NC(1) and the inset images are the FFT patterns of g-C_3N_4 and NiO.

refined fitting of Ni 2p can be attributed to Ni^{2+}, whereas the other peaks at 855.7 and 873.3 eV can be assigned to Ni^{3+} [14].

SEM and TEM images were obtained to examine the morphology. As shown in Fig. 3(a)-(b), the pristine g-C_3N_4 exhibits layer-by-layer stacked structures and the pure NiO reveals particles with an urchin structure. On the other hand, the NiO/g-C_3N_4 hybrid exhibits a flake-like shape with NiO dispersed over the g-C_3N_4 surface (Fig. 3(c)). Similar to the XPS results, only C, O, N, and Ni were observed by EDS (Fig. 3(d)). As shown in Fig. S4 and Table S3, at a low NiO ratio, the surface area increased due to less stacking of g-C_3N_4 and the reduced agglomeration of NiO particles. At an excessive NiO ratio, however, the structure became more agglomerated and the BET surface area decreased. The maximum BET surface area was as high as 54.74 m^2 g^{-1} at a melamine and $Ni(OH)_2$ precursor ratio of 1 : 1. As shown in Fig. S5, in contrast to the pristine g-C_3N_4, NC(1) exhibited type IV (Brunauer, Deming, Deming, and Teller classification) adsorption and desorption behavior, indicating that a wide range of mesopores had formed by the NiO and graphitic carbon nitride nanosheets. A well-developed porous nanostructure can promote an electrochemical reaction, kinetic reversibility, and electrolyte accessibility.

The TEM and HR-TEM (Figs. 3(e)-(f)) show that g-C_3N_4 and NiO are mixed together. The fast Fourier transform (FFT) of the selected regions clearly shows crystal planes corresponding to the (100) and (002) planes of the hexagonal graphitic carbon nitride with a lattice spacing of 2.2 and 3.4 Å, respectively [34,35]. In addition, the (200) plane of the cubic NiO phase (d=2.0 Å) [36] can be also observed.

2. Electrochemical Glucose Sensing with NiO/g-C_3N_4 Electrodes

The electrochemical active surface area (A_e) was estimated by cyclic voltammetry (CV) to evaluate the effective loading of the samples on the GC electrode surface based on the Randles-Sevcik equation [11]:

$$I_p=2.69\times10^5\cdot A_e\cdot n^{3/2}\cdot D^{1/2}\cdot v^{1/2}\cdot C \tag{I}$$

where I_p is the redox peak current (A); n is the number of electrons participating in the redox reaction (n=1); D is the diffusion coefficient of molecule (0.67×10^{-5} cm^2 s^{-1}); v is the scan rate (V s^{-1}) and C is the concentration of the redox probe molecule in solution (mol cm^3). The CV curves were obtained in a 0.2 M KCl electrolyte solution containing 5 mM $K_3(Fe(CN)_6)$ at a scan rate of 50 mV/s. A very high electrochemical active surface area was obtained from NC(1) (0.733×10^{-3} cm^2), which is five-times higher than that of g-C_3N_4 (0.146×10^{-3} cm^2) and 1.5-times higher than that of NiO (0.486×10^{-3} cm^2), suggesting the synergetic effects between NiO and g-C_3N_4 for the electrocatalytic reactions.

The electrocatalytic activities of pristine g-C_3N_4, NiO and NC(1) towards glucose were measured by CV in a 0.1 M NaOH electrolyte with and without 500 μM glucose at a scan rate of 50 mV/s. As shown in Fig. 4, the background current (without glucose) of NC(1) is higher than those of pristine g-C_3N_4 and NiO, which agrees well with the highest electrochemical surface area of NC(1). Pristine g-C_3N_4 shows no noticeable oxidation-reduction (redox) peaks both with and without glucose conditions. On the other hand, both NC(1) and NiO exhibit distinct redox peaks at +0.4 and +0.68 V,

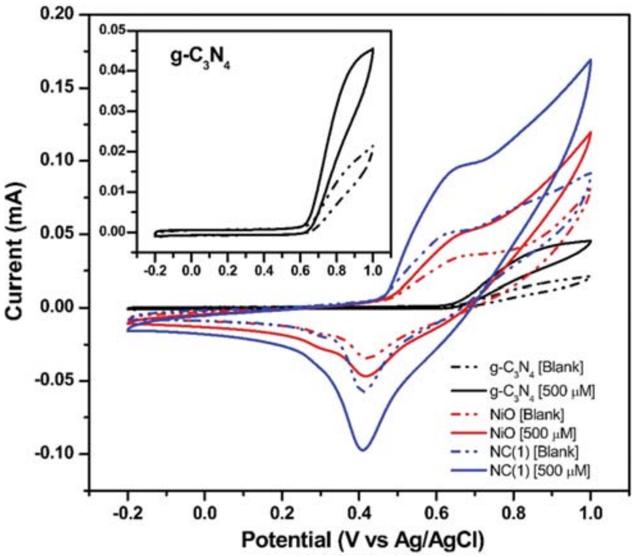

Fig. 4. CV curves of pure g-C_3N_4, NiO and NC(1) in 0.1 M NaOH at a scan rate of 50 mV/s with (solid line) and without (dash dot line) 500 μM glucose, respectively.

corresponding to Ni^{2+}/Ni^{3+} redox peaks [20]. The electrochemical oxidation of glucose on the NiO and NC(1) proceeded via two steps involving the formation of strong oxidizing species (Ni^{3+}) that are shown in the following equations:

$$NiO+OH^{-}\rightarrow NiOOH+e^{-} \tag{1}$$

$$NiOOH+glucose\rightarrow Ni(OH)_2+gluconolactone \tag{2}$$

During the anodic scan, the nickel oxyhydroxide (NiOOH) can oxidize glucose to gluconolactone, leading to an increase in current at a given potential, and likewise during the cathodic scan. The enhanced electrochemical performance of NiO/g-C_3N_4 compared to bare NiO can be attributed to the high specific surface area, high conductivity, and rapid electron transfer through the g-C_3N_4.

To explore the electrochemical redox process, the change in current at various scan rates was studied in the presence of 1 mM glucose. Obviously, the current increased and the peak shifted slightly to a higher potential with increasing scan rate. Fig. S6 shows the linear relationship between the currents of the both anodic (oxidation) and cathodic (reduction) peak of NC(1) and the square root of the scan rate in the range of 10-100 mV/s with a correlation coefficient (R^2) of 0.9998 (I_{pa}) and 0.9984 (I_{pc}), respectively, suggesting that the glucose redox reaction is a typical diffusion-controlled process with rapid electron-transfer from the electrolyte to the electrode surface [37], involving OH- diffusion from the electrolyte to the electrode surface during the reduction step and from the electrode to the electrolyte during the oxidation step [38]. Furthermore, the increase of the peak current with the scan rate confirms the oxidation of glucose on the NiO/g-C_3N_4, which proceeds via surface-controlled electrochemical reactions by the adsorption of glucose and oxidized intermediates [39].

Fig. 5(a) shows the CV curves of the NC(1) electrode at various glucose concentrations. The redox peak currents increased gradually with increasing glucose concentration, whereas the peak poten-

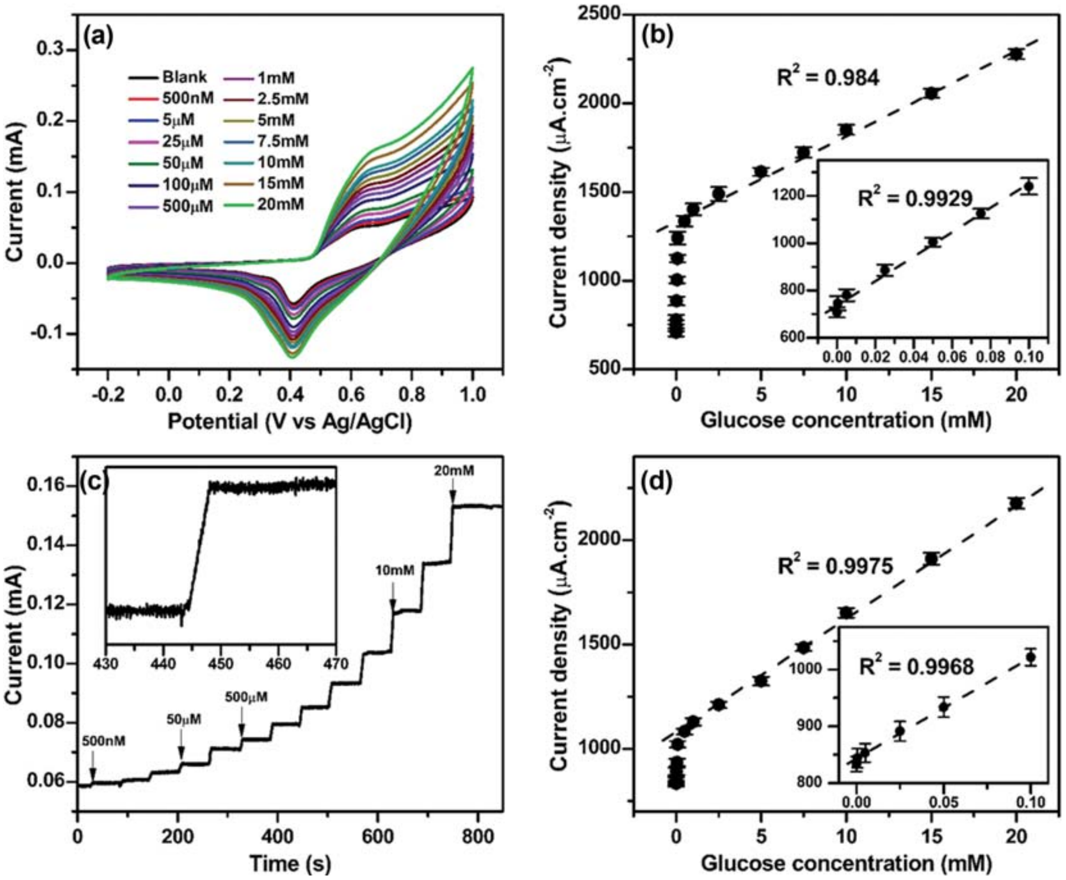

Fig. 5. (a) CV curves of the NC(1) and (b) calibration curve from CV of NC(1) at a wide range of glucose concentrations from 500 nM to 20 mM. (c) Typical amperometric current response recorded at +0.68 V and (d) calibration curves vs. glucose concentration from amperometric with the successive addition of various glucose concentrations at 60 s intervals.

tial shifted slightly positively for the oxidation peak and negatively for the reduction peak. This can be attributed to the diffusion controlled reaction at high glucose concentrations, which reveals the excellent electrocatalytic activity of the NiO/g-C_3N_4 fabricated in this study [40].

Fig. 5(b) presents the calibration curve of the anodic peak current with the concentration of glucose obtained from the CV curves in Fig. 5(a); two linear relationships were defined in the ranges, 500 nM-100 μM and 100 μM-20 mM. The slope of linear range was obtained corresponding to the sensitivity towards glucose. Then, the sensor based on the NC(1) electrode exhibited a sensitivity as high as 5,387.1 μA mM^{-1} cm^{-2} , which is one of the highest values ever reported (Table S4), as well as a limit of detection (LOD) of 2.30 μM (S/N=3). Table S3 and Fig. S7 show the sensitivity towards glucose of pristine g-C_3N_4, NiO and various NC(x).

As summarized in Table S3, NC(1) exhibited ~5.5 and ~28 times higher sensitivity than those of pristine NiO and g-C_3N_4, which indicates the synergetic effects between them, such as high surface area, enhanced conductivity, and effective charge transfer. As described in the BET results, the sensitivity decreases at an excessively high NiO ratio, which can be due to the agglomeration of NiO particles.

The amperometric response of the NC(1) electrode towards glucose was monitored under a constant potential of +0.68 V with the successive injection of various glucose concentrations into the 0.1 M NaOH electrolyte at 60 s intervals. As shown in Fig. 5(c), during the successive addition of glucose, a well-defined, stable, and rapid response (<4 s) of NC(1) towards glucose is observed. The amperometric response exhibits a step-like increase in current and a rapid steady-state current upon the addition of glucose. The calibration curve obtained from the amperometric test (Fig. 5(d)) also exhibits excellent linearity and sensitivity as it did from the CV curves.

3. Stability, Reproducibility and Anti-interference Property of the NiO/g-C_3N_4 Electrode

The stability of the NiO/g-C_3N_4-based glucose sensor was examined by measuring its current change towards glucose for a 30 day period. The sensor was exposed to air at room temperature, and its sensitivity was obtained every three days. The current of NC(1) decreased to only 8% compared to its original current after 30 days (Fig. S8) and the slope became smaller, suggesting that NiO/g-C_3N_4 has good stability under ambient conditions. In addition, the XRD patterns of NiO/g-C_3N_4 before and after 30 days test (Fig. S9) are almost the same, which indicates that there is no notable structural change even after 30 days stability test. The reproducibility of NiO/g-C_3N_4 was also evaluated by amperometric test three times, with a relative standard deviation (RSD) of 1.53%. In addition, twelve measurements of glucose on one electrode were taken upon the sequential addition of 1.0 mM glucose in 0.1 M NaOH. The RSD was 2.76%, which confirmed that the NiO/g-C_3N_4 fabricated in this study exhibited excellent reproducibility and reliability.

The selectivity of NiO/g-C_3N_4 was examined by adding interference species, including dopamine, ascorbic acid (AA), uric acid (UA), sorbitol, glycine, l-cystine, and other carbohydrate compounds, to the solution. Because the concentration of glucose in human serum is higher than those of the interference species [20,41,42], an anti-interference test was performed by the successive addition of 1.0 mM glucose and 0.1 mM of various interfering species, respectively. As shown in Fig. S10, NC(1) exhibits a negligible response towards all interfering species, which indicates the excellent selectivity towards NiO/g-C_3N_4 fabricated in this study.

4. Real Sample Test

To evaluate the feasibility of monitoring the glucose level in the in real blood, the amperometric response of NiO/g-C_3N_4 was recorded with the addition of horse and rabbit blood serum, whose glucose concentration was already known from the provider. As shown in Fig. S11, the current increased linearly with increasing concentration of serum. To evaluate the accuracy of NiO/g-C_3N_4, the glucose concentration in real blood serum was compared with that using a commercial glucometer. Table 1 lists the glucose concentration for real blood serum obtained using both a commercial ACCU-CHEK® Performa Blood Glucose Meter and NiO/g-C_3N_4-based glucose sen-

Table 1. Comparison of the glucose level between NiO/g-C_3N_4 and commercial glucometer

Dilution ratio of serums in DI water	Horse blood serum (mM)		Rabbit blood serum (mM)	
	NiO/g-C_3N_4	Glucometer	NiO/g-C_3N_4	Glucometer
Pure	3.331	3.385	6.200	6.161
1 : 1	1.964	1.942	3.420	3.497
1 : 2	1.428	1.443	2.720	2.664
1 : 3	0.879	0.888	2.092	2.054
Error (%)	1.761		3.722	

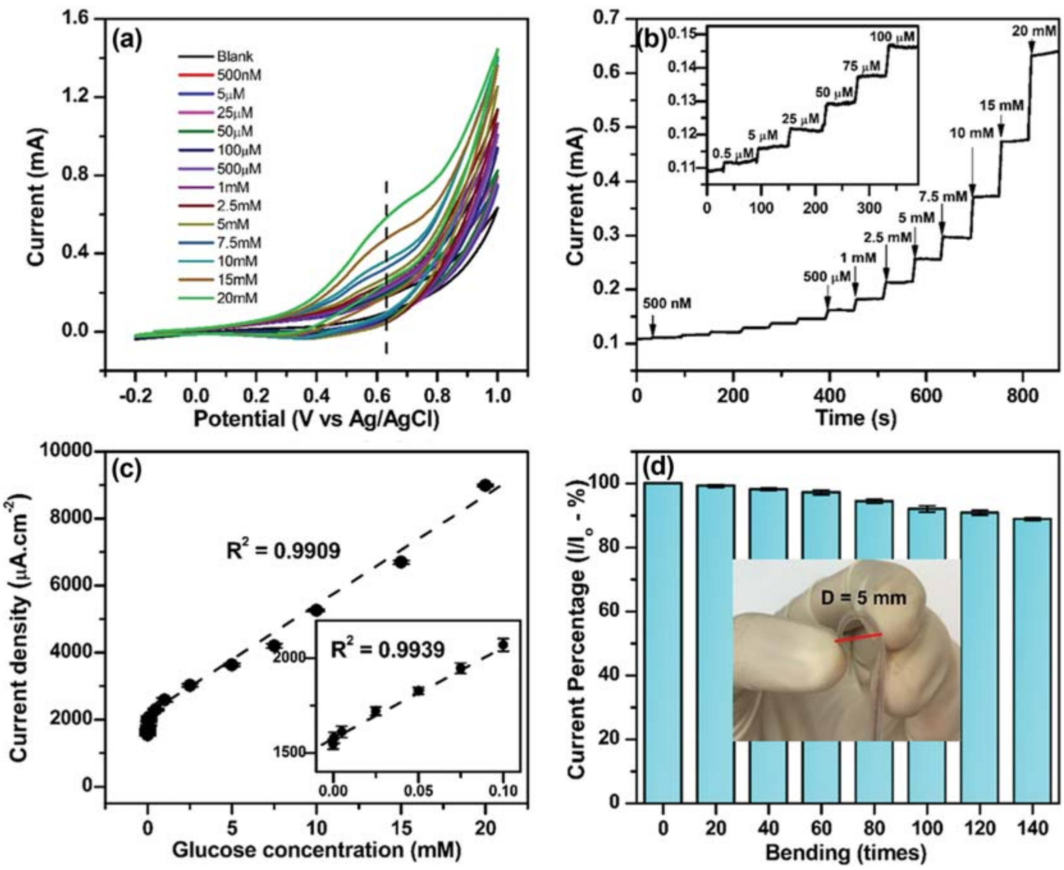

Fig. 6. (a) CV test of NC(1)/flexible electrode in the presence of various glucose concentrations in 0.1 M NaOH at a scan rate of 50 mV/s. (b) Amperometric response of NC(1)/flexible sensor at +0.64 V with the successive addition of glucose in 0.1 M NaOH at every 60 s. (c) Calibration curve of NC(1)/flexible sensor with the linear fitting result. (d) Current response with different bending times in 0.1 M NaOH. The inset shows a digital picture of a bent NC(1) electrode.

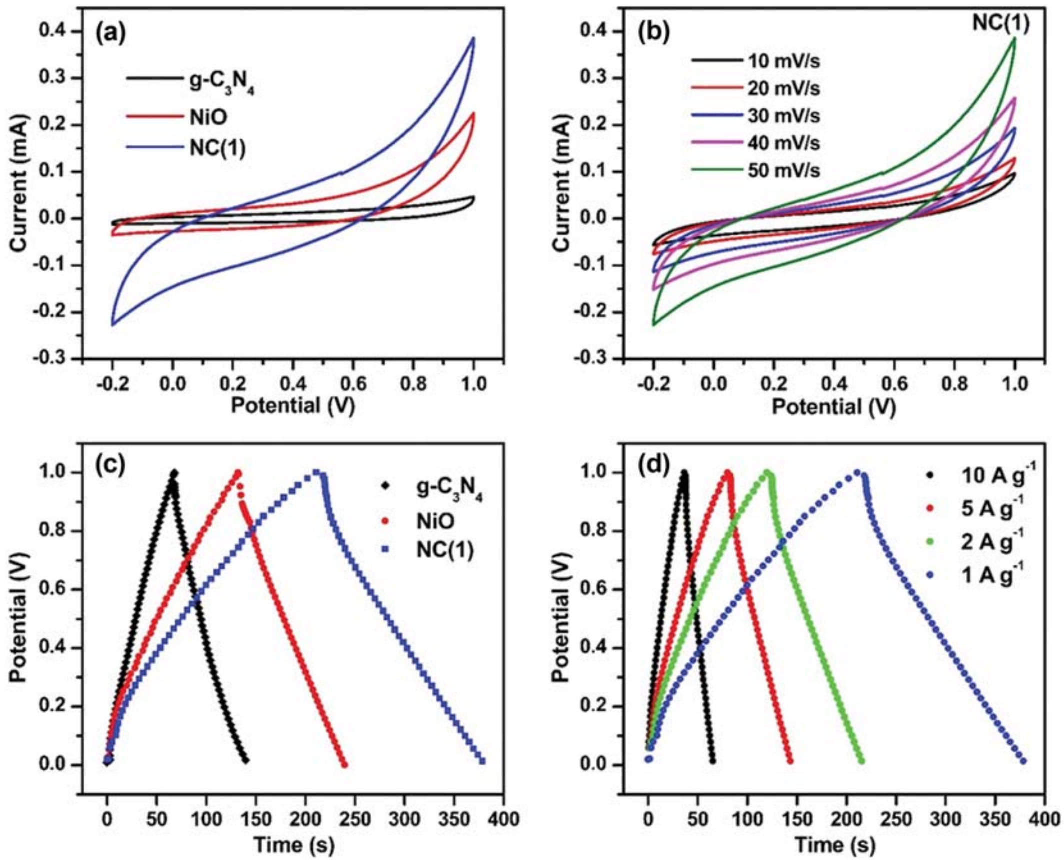

Fig. 7. (a) CV curves of g-C_3N_4, NiO and NC(1) at scan rate of 50 mV/s. (b) CV curves of NC(1) at different scan rates. (c) CD curves of g-C_3N_4, NiO and NC(1) at a constant current density of 1 A g^{-1}. (d) CD curves of NC(1) at various current density varying from 1 to 10 A g^{-1}.

sor. The mean difference was only 1.76% for HS and 3.72% for RS, which demonstrates that NiO/g-C_3N_4 fabricated in this study shows comparable glucose sensing capability to that of a commercial enzymatic glucometer.

5. Flexible Glucose Sensor Based on NiO/g-C_3N_4

The NiO/g-C_3N_4 flexible glucose sensor was fabricated on PDMS and Cu foil, as shown in Fig. S12. The electrocatalytic properties of NC(1) on a flexible electrode were investigated by CV in 0.1 M NaOH at a scan rate of 50 mV/s. As shown in Fig. 6(a), it exhibits significant redox peaks in the presence of glucose at approximately +0.64 V and +0.34 V, which is in agreement with the NiO/g-C_3N_4 on the GCE electrode. The sensitivity and linear range of the fabricated flexible electrochemical sensor in response to various glucose concentrations from 500 nM to 20 mM at an applied potential of +0.64 V were investigated using amperometry, as shown in Fig. 6(b). After injecting glucose, the current also increased immediately and maintained a stable current. The sensitivity and LOD of NC(1) on the flexible electrode calculated from the calibration curve shown in Fig. 6(c) were 5,001.9 μA mM^{-1} cm^{-2} and 5.1 mM, respectively, which are similar to those of NiO/g-C_3N_4 on the GCE electrode. To evaluate the resistance to the physical stress environment, the current was measured after performing the bending test 140 times (Fig. 6(d)). The bending radius was 5 mm and bending was focused on the NiO/g-C_3N_4 part of the entire flexible electrode. There was no significant change after bending 40 times and ~88.9% of the initial current was maintained after bending 140 times, which implies that NiO/g-C_3N_4 flexible glucose sensor can be used effectively in the wearable healthcare devices that can be exposed to frequent physical stress conditions.

6. Electrochemical Capacitance Behavior

The electrochemical performance of pristine g-C_3N_4, NiO, and NC(1) as a supercapacitor electrode was examined by CV, galvanostatic charge-discharge (CD), and electrochemical impedance spectroscopy (EIS). As shown in Figs. 7(a) and 7(c), NC(1) exhibits highly enhanced capacitance compared to those of pristine g-C_3N_4 and NiO. The specific capacitances of g-C_3N_4, NiO, and NC(1) calculated from the CV curves (Figs. 7(b) and S13(a)-(b)) and CD curves (Fig. 7(c)) were 105.6 and 110.7, 220.2 and 223.2, and 344.2 and 357.1 F g^{-1}, respectively, at a scan rate of 50 mV/s and constant current density of 1 A g^{-1}. The electrolyte resistance, mass transfer, mass transport kinetics and electric double layer played important role during the process with might distort the CV curve [43]. Moreover, Eqs. (S1) and (S2) show that apart from the integrated area, other factor responsible for slope of the discharge curve, so the capacitance value from two different equations varies in a little amount. The IR drop was observed at the start of all discharge curves at a high current density (Fig. 7(d)), indicating good contact between the NC(1) and Cu electrode, as well as rapid and reversible diffusion of the electrolyte. NC(1) shows ~1.7 and ~3.3-fold enhanced capacitance compared to those of the pristine NiO and g-C_3N_4, which can be attributed to the increased BET surface area and faster charge transfer.

EIS was performed over the frequency range, 0.01 Hz-1,000 kHz, to analyze the resistance of the g-C_3N_4, NiO and NC(1) electrodes. As shown in the Nyquist plot (Fig. S13(c)), a slight semicircle arc is observed at the high frequency region and a line slightly tilted at an angle of 30° towards Z′ axis is noted at the low frequency region. The intercept at the real axis in the high frequency represents the ohmic resistance (R_s), which is the combined electrolyte solution resistance, electronic resistance, and contact resistance. The diameter of the semicircle loop represents the charge transfer resistance (R_{ct}), which can be obtained directly. The line at the middle and low frequency originates from the diffusion of the electrolyte to the electrode surface, which is the Warburg impedance [23,44]. NC(1) shows a lower R_s (2.8 Ω) value than those of the NiO (3.7 Ω) and g-C_3N_4 (7.5 Ω) electrodes. Moreover, the fitted R_{ct} value of NC(1) (4.7 Ω) is smaller than that of NiO (~11 Ω), which indicates that NC(1) has higher conductivity than pristine NiO. The electrochemical performance of NiO was obviously improved because of the introduction of g-C_3N_4.

A Ragone plot was used to correlate the energy density and power density to evaluate the performance of the supercapacitors. NC(1) showed the maximum energy density of 49.6 Wh kg^{-1} at a power density of 1,064.2 W kg^{-1} with a current density of 1 A g^{-1}, which is one of the highest values among those reported elsewhere as shown in Fig. S14. In addition, the energy density maintained a high value of 40.5 Wh kg^{-1}, even at a high power density of 5,042.9 W kg^{-1} (current density at 10 A g^{-1}), suggesting that the NiO/g-C_3N_4 fabricated in this study can be used effectively in energy storage devices. The cycling stability of NC(1) was evaluated by 1,000 CD cycles at a current density of 1 A g^{-1}. As shown in Fig. S13(d), NC(1) retained ~92.2% of its initial capacitance after 1,000 cycles. The NC(1)-based supercapacitor alone could turn on a light-emitting-diode (Fig. S15).

7. Self-powered Glucose Sensor

To evaluate the multi-functional characteristics of NiO/g-C_3N_4 fabricated in this study, the feasibility of a NC(1) supercapacitor powered glucose sensor was tested. As shown in Fig. S16, NC(1) was used as both a glucose sensing material and supercapacitor electrode. The system included three main parts, power supply, supercapacitor, and glucose sensor. First, the NC(1) supercapacitor was charged by the power supply at 2.0 V for 50 s. Subsequently, the power supply was turned off and the NC(1) glucose sensor was then operated by only the NC(1) supercapacitor. The current obtained from the amperemeter was 0.020 mA without glucose (Fig. S16(c)), which increased to 0.038 mA immediately after adding 1 mM glucose (Fig. S16(d)). Therefore, this can open a new way to build a very simple glucose sensor system that can use the same material for associated the power supply and sensing devices. In practical application, a flexible electrode can be used instead of glassy carbon electrode and a portable device can be designed as shown in Fig. S16(a).

CONCLUSIONS

A multi-functional NiO/g-C_3N_4 hybrid nanostructure was fabricated by a hydrothermal process followed by thermal treatment. The as-synthesized NiO/g-C_3N_4 exhibited excellent glucose sensing and supercapacitor properties because of the synergetic effects between them, such as improved electrical conductivity and formation of a porous three-dimensional structure. The NiO/g-C_3N_4-based glucose sensor exhibited an excellent sensitivity, as high as 5,387.1 μA mM^{-1} cm^{-2}, wide linear range, low detection limit, rapid response, and high stability. In addition, it exhibited excellent anti-interference properties, mechanical flexibility, and allowed precise monitoring of the glucose level even real blood serum. Furthermore, NiO/g-C_3N_4 showed high capacitance and long-term cycling stability when used as a supercapacitor electrode, which makes it possible to construct a very simple glucose sensor system that uses the same material (NiO/g-C_3N_4) for both the power supply and sensing devices.

ACKNOWLEDGEMENTS

This study was supported by the Basic Science Research Program through the National Research Foundation of Korea (NRF) funded by The Ministry of Science, ICT and Future Planning (2019R1A2B5B02069683).

SUPPORTING INFORMATION

Additional information as noted in the text. This information is available via the Internet at http://www.springer.com/chemistry/journal/11814.

REFERENCES

1. D.-W. Hwang, S. Lee, M. Seo and T. D. Chung, *Anal. Chim. Acta*, **1033**, 1 (2018).
2. S. A. Shabbir, S. Tariq, M. G. B. Ashiq and W. A. Khan, *Biosci. Rep.*, **39**, BSR20181983 (2019).
3. M. Christwardana, J. Ji, Y. Chung and Y. Kwon, *Korean J. Chem. Eng.*, **34**, 2916 (2017).
4. L. C. Clark and C. Lyons, *Ann. N.Y. Acad. Sci.*, **102**, 29 (1962).
5. Y. Su, H. Guo, Z. Wang, Y. Long, W. Li and Y. Tu, *Sens. Actuators, B: Chem.*, **255**, 2510 (2018).
6. M. Christwardana, Y. Chung, D. C. Tannia and Y. Kwon, *Korean J. Chem. Eng.*, **35**, 2421 (2018).
7. J. Chen, C. Liu, Y.-T. Huang, H. Lee and S.-P. Feng, *Nanotechnology*, **29**, 505501 (2018).
8. Y. Li, Y.-Y. Song, C. Yang and X.-H. Xia, *Electrochem. Commun.*, **9**, 981 (2007).
9. Y.-Y. Song, D. Zhang, W. Gao and X.-H. Xia, *Chem. Eur. J.*, **11**, 2177 (2005).
10. S. Liu, B. Yu and T. Zhang, *Electrochim. Acta*, **102**, 104 (2013).
11. P. Zhang, L. Zhang, G. Zhao and F. Feng, *Microchim. Acta*, **176**, 411 (2012).
12. L. T. Hoa, J. S. Chung and S. H. Hur, *Sens. Actuators, B: Chem.*, **223**, 76 (2016).
13. Y.-L. T. Ngo, L. T. Hoa, J. S. Chung and S. H. Hur, *J. Alloys Compd.*, **712**, 742 (2017).
14. Y.-L. T. Ngo, L. Sui, W. Ahn, J. S. Chung and S. H. Hur, *Nanoscale*,

9, 19318 (2017).
15. N. Pal, S. Banerjee and A. Bhaumik, *J. Colloid Interface Sci.*, **516**, 121 (2018).
16. M. Baghayeri, A. Amiri, Z. Alizadeh, H. Veisi and E. Hasheminejad, *J. Electroanal. Chem.*, **810**, 69 (2018).
17. H. M. Shiri and M. Aghazadeh, *J. Electrochem. Soc.*, **159**, E132 (2012).
18. C. Heyser, R. Schrebler and P. Grez, *J. Electroanal. Chem.*, **832**, 189 (2019).
19. M. El-Kemary, N. Nagy and I. El-Mehasseb, *Mater. Sci. Semicond. Process.*, **16**, 1747 (2013).
20. Y. Zhang, Y. Wang, J. Jia and J. Wang, *Sens. Actuators, B: Chem.*, **171-172**, 580 (2012).
21. S. Zhang, J. Li, M. Zeng, J. Xu, X. Wang and W. Hu, *Nanoscale*, **6**, 4157 (2014).
22. M. K. Kundu, M. Sadhukhan and S. Barman, *J. Mater. Chem., B*, **3**, 1289 (2015).
23. H.-L. Zhu and Y.-Q. Zheng, *Electrochim. Acta*, **265**, 372 (2018).
24. Q. Liang, L. Ye, Q. Xu, Z.-H. Huang, F. Kang and Q.-H. Yang, *Carbon*, **94**, 342 (2015).
25. J. Chen, Z. Mao, L. Zhang, D. Wang, R. Xu, L. Bie and B. D. Fahlman, *ACS Nano*, **11**, 12650 (2017).
26. A. Wang, C. Wang, L. Fu, W. Wong-Ng and Y. Lan, *Nano-Micro Lett.*, **9**, 47 (2017).
27. S. An, G. Zhang, T. Wang, W. Zhang, K. Li, C. Song, J. T. Miller, S. Miao, J. Wang and X. Guo, *ACS Nano*, **12**, 9441 (2018).
28. T.-T. Pham and E. W. Shin, *Langmuir*, **34**, 13144 (2018).
29. J. Ehrmaier, T. N. V. Karsili, A. L. Sobolewski and W. Domcke, *J. Phys. Chem. A*, **121**, 4754 (2017).
30. Z. Wei, M. Liu, Z. Zhang, W. Yao, H. Tan and Y. Zhu, *Energy Environ. Sci.*, **11**, 2581 (2018).
31. I. S. Pieta, A. Rathi, P. Pieta, R. Nowakowski, M. Hołdynski, M. Pisarek, A. Kaminska, M. B. Gawande and R. Zboril, *Appl. Catal. B*, **244**, 272 (2019).
32. Y.-L. T. Ngo, J. S. Chung and S. H. Hur, *Dyes Pigm.*, **168**, 180 (2019).
33. F. Motahari, M. R. Mozdianfard and M. Salavati-Niasari, *Process Saf. Environ.*, **93**, 282 (2015).
34. Y.-L. T. Ngo, W. M. Choi, J. S. Chung and S. H. Hur, Sens. *Actuators, B: Chem.*, **282**, 36 (2019).
35. N. Cheng, P. Jiang, Q. Liu, J. Tian, A. M. Asiri and X. Sun, *Analyst*, **139**, 5065 (2014).
36. S. Rakshit, S. Ghosh, S. Chall, S. S. Mati, S. P. Moulik and S. C. Bhattacharya, *RSC Adv.*, **3**, 19348 (2013).
37. T. Marimuthu, S. Mohamad and Y. Alias, *Synth. Met.*, **207**, 35 (2015).
38. P. Subramanian, J. Niedziolka-Jonsson, A. Lesniewski, Q. Wang, M. Li, R. Boukherroub and S. Szunerits, *J. Mater. Chem. A*, **2**, 5525 (2014).
39. M. Li, X. Bo, Z. Mu, Y. Zhang and L. Guo, *Sens. Actuators, B: Chem.*, **192**, 261 (2014).
40. J. Yang, M. Cho, C. Pang and Y. Lee, *Sens. Actuators, B: Chem.*, **211**, 93 (2015).
41. M. Wu, S. Meng, Q. Wang, W. Si, W. Huang and X. Dong, *ACS Appl. Mater. Interfaces*, **7**, 21089 (2015).
42. R. A. Soomro, Z. H. Ibupoto, Sirajuddin, M. I. Abro and M. Willander, *Sens. Actuators, B: Chem.*, **209**, 966 (2015).
43. M. S. Palagonia, C. Erinmwingbovo, D. Brogioli and F. La Mantia, *J. Electroanal. Chem.*, **847**, 113170 (2019).
44. A. Roy, A. Ray, S. Saha, M. Ghosh, T. Das, B. Satpati, M. Nandi and S. Das, *Electrochim. Acta*, **283**, 327 (2018).

Supporting Information

Multi-functional NiO/g-C_3N_4 hybrid nanostructures for energy storage and sensor applications

Yen-Linh Thi Ngo, Jin Suk Chung†, and Seung Hyun Hur†

School of Chemical Engineering, University of Ulsan, Daehak-ro 93, Nam-gu, Ulsan 44610, Korea

(*Received 30 December 2019 • Revised 19 January 2020 • Accepted 28 February 2020*)

1. Materials

Nickel (II) chloride hexahydrate ($NiCl_2{\cdot}6H_2O$), urea ($CO(NH_2)_2$), melamine, sodium hydroxide (NaOH), ethanol 99.9% (C_2H_5OH), nafion, isopropanol (IPA), carbon (C), D-(+)-glucose, D-(−)-fructose, maltose, lactose, galactose, sucrose, l-cystine (L-cys), glycine (Glys), ascorbic acid (AA), uric acid (UA), sorbitol (Sor), dopamine (DA), horse serum (HS), and rabbit serum (RS) were purchased from Sigma-Aldrich Co. (USA). All reagents were used as received. Deionized (DI) water was used throughout the experiments.

2. Instruments

Field-emission scanning electron microscopy (FE-SEM, JSM-7600F, JEOL, Japan) was carried out at an acceleration voltage of 15 kV. High-resolution transmission electron microscopy (HR-TEM, JEM-2100F, JEOL, USA) images were performed at an accelerating voltage of 100 kV. Fourier transform infrared (FT-IR, Nicolet 380, iS5, Thermo Fisher, USA) spectroscopy was conducted. X-ray diffraction (XRD, Rigaku, Japan) was performed using Cu Kα radiation. X-ray photoelectron spectroscopy (XPS, ESCALAB 250Xi, Thermo Fisher Scientific, USA) was conducted using an Al Kα X-ray source. Thermogravimetric analysis (TGA, TGA Q50, TA Instruments, USA) was carried out in the nitrogen environment. The specific surface area was measured by nitrogen adsorption/desorption isotherm analysis on a Micromeritics ASAP 2020 (USA) apparatus and calculated using the Brunauer-Emmett-Teller (BET) method. The voltage amplitude in an electronic circuit was identified using a Tektronix digital oscilloscope (TDS 210). A handheld digital multimeter (EZ Digital DM-332) was used to measure the DC current and the DC power supply used was a 4-channel 200 W GW INSTEK (GPS-4303).

All electrochemical measurements for glucose sensing were performed on an electrochemical workstation (Bio Logic, SP-50, USA) in a standard three-electrode cell. The NC/GCE was used as the

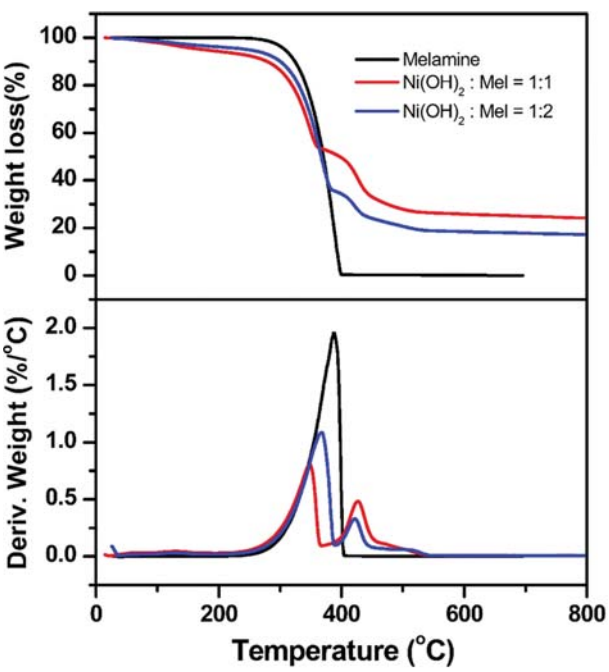

Fig. S1. Thermal treatment process was simulated under nitrogen flow gas by TGA (top) and (DTA) analyses for melamine and as-synthesized NiO/g-C_3N_4 composites.

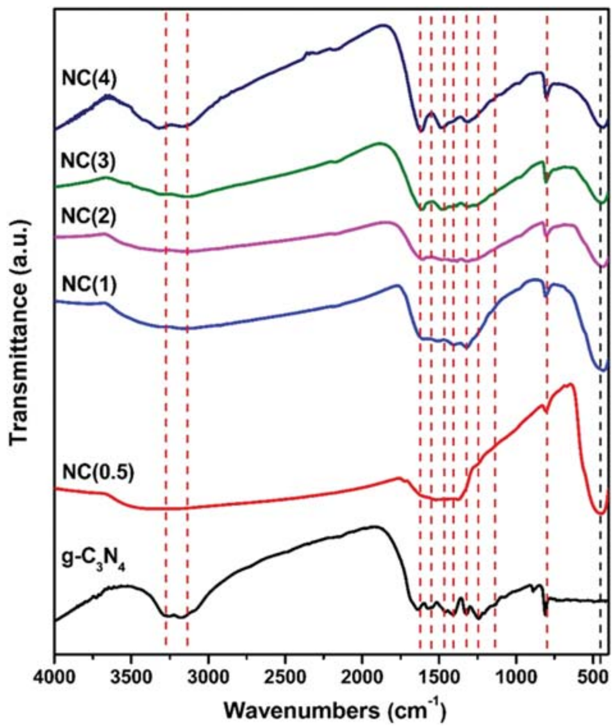

Fig. S2. FT-IR spectra of pure g-C_3N_4 and NC(x) with various $Ni(OH)_2$ and melamine mass ratios.

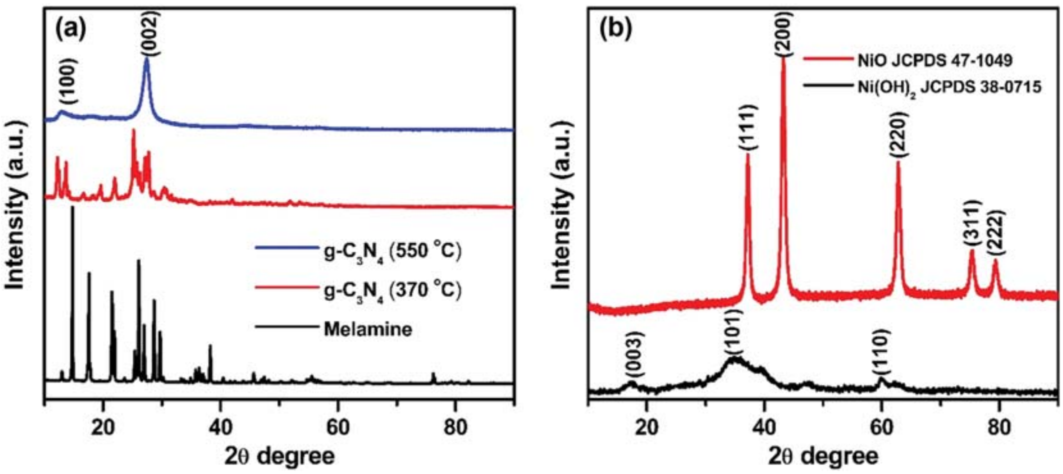

Fig. S3. XRD patterns of (a) melamine, g-C_3N_4 calcinated at 370 and 500 °C; (b) $Ni(OH)_2$ and NiO.

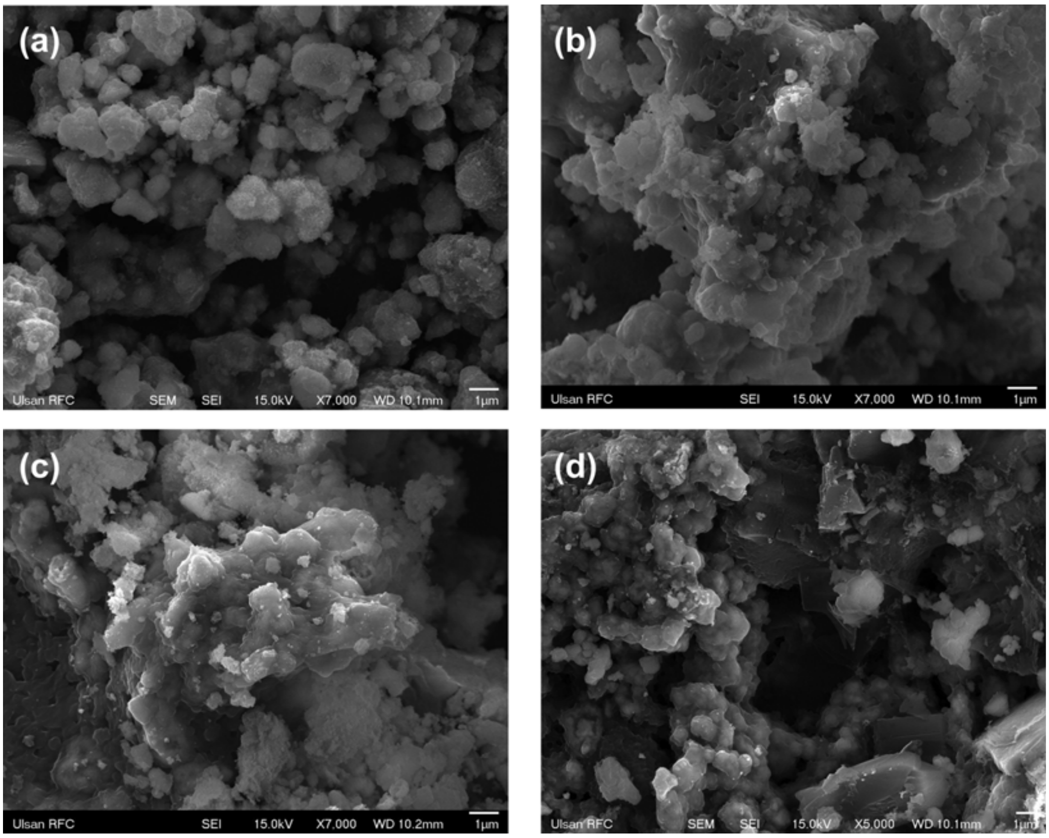

Fig. S4. FE-SEM images of various composite (a) NC(0.5), (b) NC(2), (c) NC(3) and (d) NC(4).

working electrode with a platinum wire and Ag/AgCl as the counter and reference electrodes, respectively. The measurements for the glucose sensor were carried out in a 0.1 M NaOH solution at room temperature. In the capacitance experiments, the measurements were carried out using two symmetric electrodes in a 2 M KOH electrolyte, as shown in Scheme 1.

3. Equation to Calculated the Specific Capacitance, Energy Density and Power Denstiy

The specific capacitance was calculated by both cyclic voltammetry (CV) and galvanostatic charge-discharge (CD) using the following equations, respectively [1]:

$$C_{S,\,CV} = \frac{\int IdV}{2 \times m \times \Delta V \times S} \quad \text{(S1)}$$

where $C_{S,CV}$ is the specifice capacitance obtained from CV (F g^{-1}); $\int IdV$ is the integrated area of the CV curve; m is the mass of the single electrode (g); ΔV is the potential window (V); and S is the scan rate (V s^{-1}).

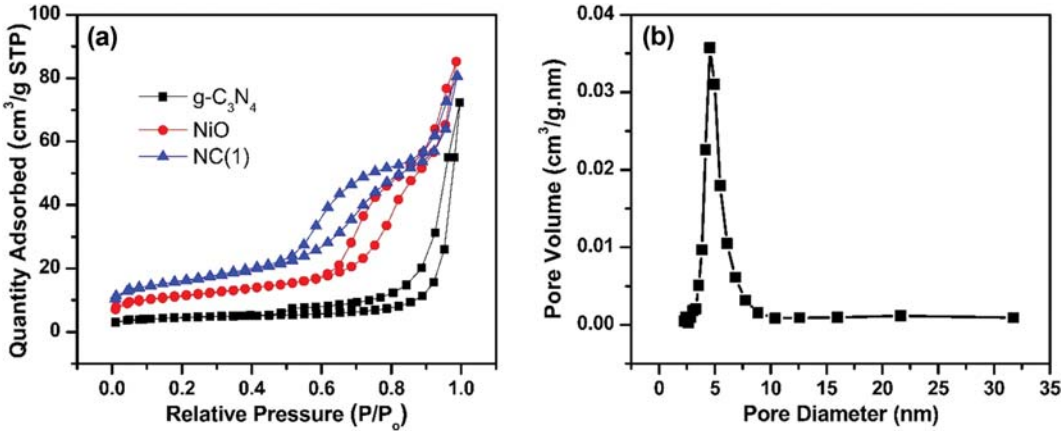

Fig. S5. (a) N_2 adsorption-desorption (BET isotherm) of g-C_3N_4. NiO, and NC(1); (b) BJH pore size distribution of NC(1).

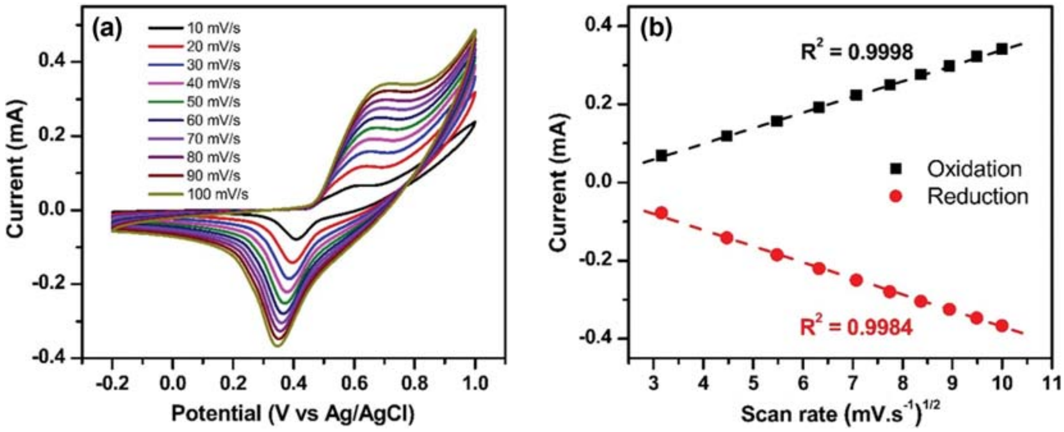

Fig. S6. (a) CV curves of the NC(1) in 0.1 M NaOH with 1 mM glucose at different scan rates 10-100 mV/s. (b) Plot of the peak current versus the square root of the scan rate at an applied potential of +0.68 V.

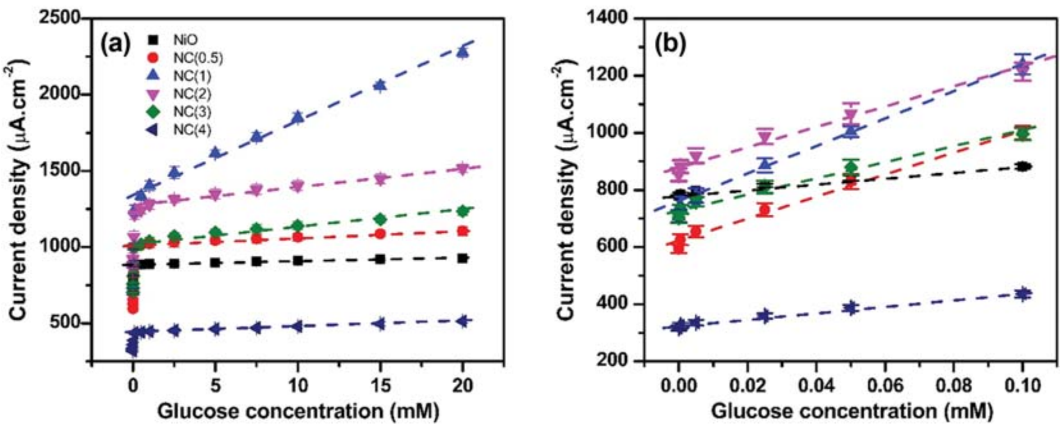

Fig. S7. Plot of calibration curves of NiO and composites NC(x) with (a) various glucose concentration and (b) low glucose concentration (from 0-0.1 mM) in 0.1 M NaOH at a scan rate of 50 mV/s.

$$C_{S,\,CD} = \frac{I}{m \times \left(\frac{dV}{dt}\right)} \tag{S2}$$

where $C_{S,CD}$ is the specifice capacitance obtained from CD (F g^{-1}); I is the constant charge/discharge current (A); m represents the total mass active material (g); and dV/dt is the slope of the discharge curve.

Energy density (E) and power density (P) derived from galvanostatic tests can be calculated from the following equations [2,3]:

$$E = \frac{1}{2}\left[\frac{C(\Delta V)^2}{3.6}\right] \tag{S3}$$

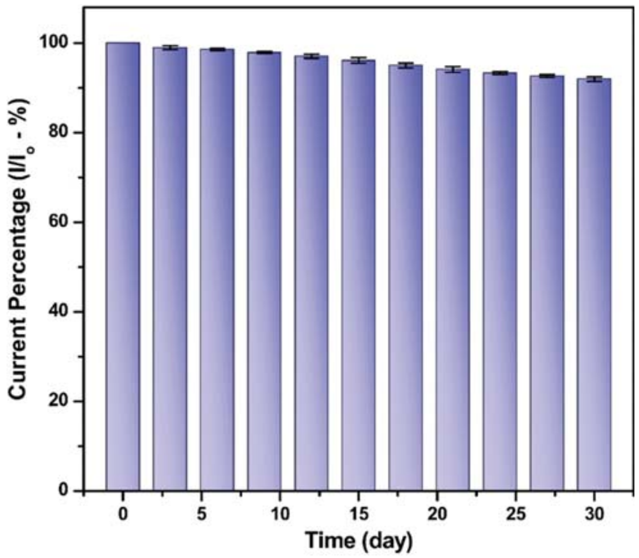

Fig. S8. **Stability of NC(1) based glucose sensor at room temperature. The current was recorded every 3 days in 30 days.**

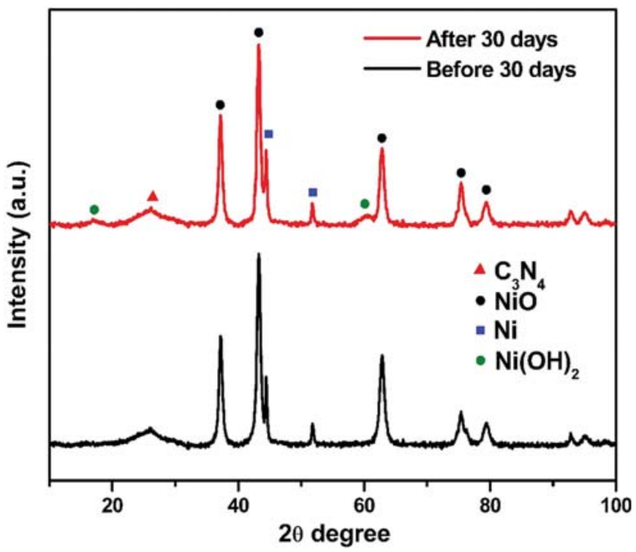

Fig. S9. **XRD patterns of NiO/g-C_3N_4 before and after 30 days stability test.**

$$P = \frac{3600 \times E}{\Delta t} \tag{S4}$$

where E is the energy density (Wh kg^{-1}); C is specific capacitance (F g^{-1}); V is discharge potential; P is the power density (W kg^{-1}); and Δt is discharge time (h), respectively.

4. The Process of Self-supply Power for the Glucose Sensor and LED

The NiO/g-C_3N_4 composite was used as both electrodes for glucose sensor and supercapacitor (SC) - energy storage devices. Firstly, the SC was charged by the DC power supply laboratory turned on at 2.0 V. After that, the DC power would be disconnected when the SC was full and stable after about 50 s and its be using this power to apply for the glucose sensor. The current was obtained at 0.67 V before adding glucose is 0.020 mA. Finally, glucose was adding and the current recorded at 0.038 mA. Moreover, the SC was also used as a power supply source, which could supply power for LED after charging as shown in Fig. S12.

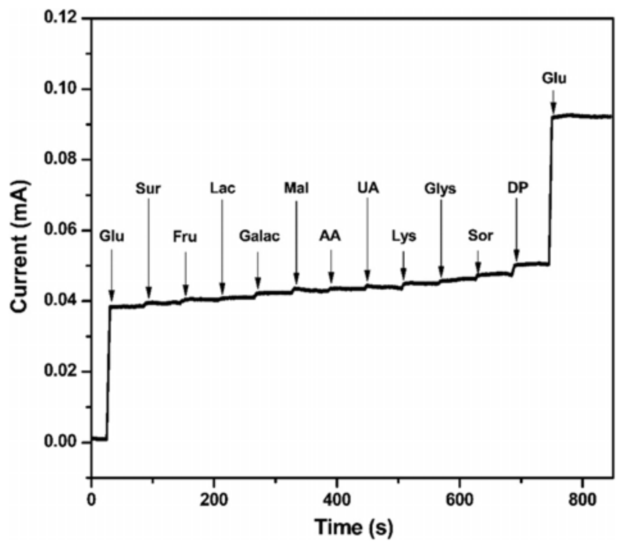

Fig. S10. **Typical amperometric response of NC(1) to the sequential addition of 1 mM glucose and 0.1 mM interferents of UA, AA, Sor, DP, Lys, Glys, galactose, fructose, lactose, maltose, and sucrose in 0.1 M NaOH electrolyte at an applied voltage of +0.68 V.**

Table S1. Relative ratio of C=C, HC-O, N-C=N and N-C=O/O-C=O of all samples by C 1s spectra analysis

Sample	C=C		O-C-O		N-C=N		O-C=O/N-C=O	
	Area	%	Area	%	Area	%	Area	%
g-C_3N_4	965.31	7.54	820.06	6.41	1,0057.44	78.57	957.01	7.48
NC(1)	922.17	17.03	894.45	16.52	221.69	40.84	1,387.43	25.61

Table S2. Relative ratio of C-N=C (N_1), N-$(C)_3$ and HN-$(C)_2$ (tertiary - N_2), C - NH (quaternary - N_3) of all samples by N 1s spectra analysis

Sample	N_1		N_2		N_3		π-π Excitation	
	Area	%	Area	%	Area	%	Area	%
g-C_3N_4	21,157.44	59.90	6,109.12	17.30	5,976.63	16.92	2,079.04	5.89
NC(1)	2,045.90	49.70	1,064.20	25.85	707.00	17.17	299.47	7.28

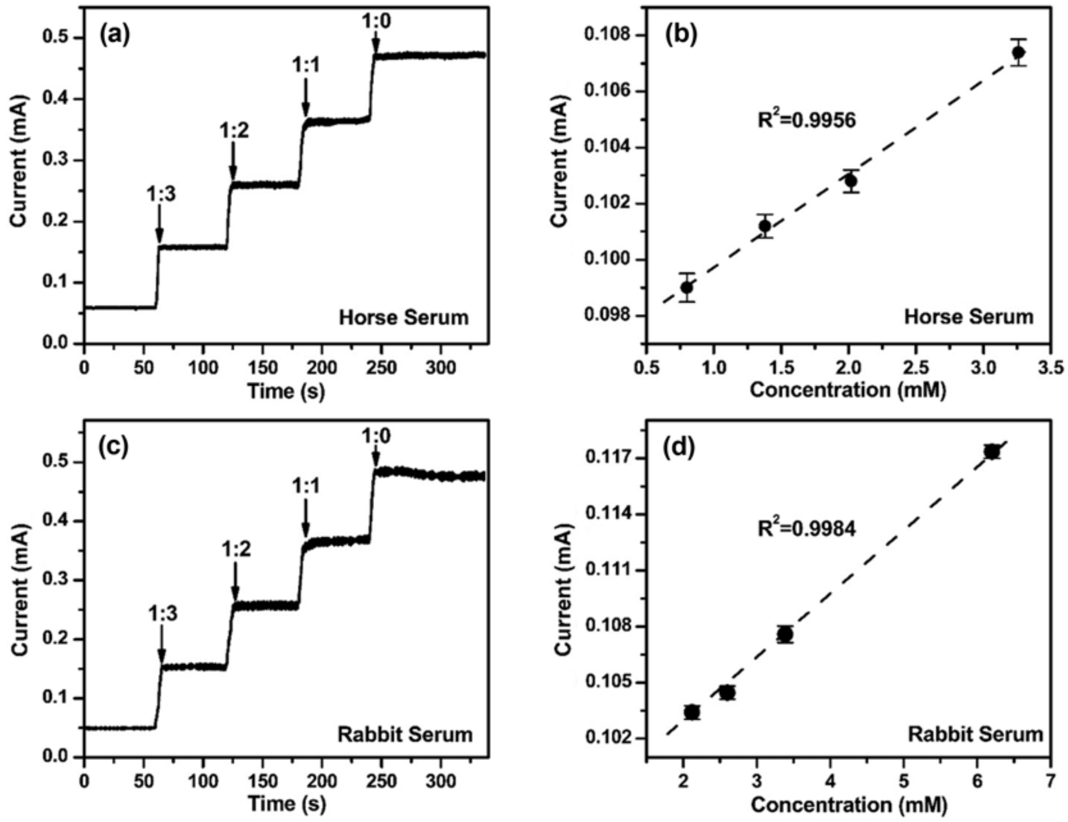

Fig. S11. Amperometric tests and calibration cures of NC(1) in 0.1 M NaOH at an applied potential +0.68 V with the successive addition real serum samples (a)-(b) Horse serum and (c)-(d) Rabbit serum.

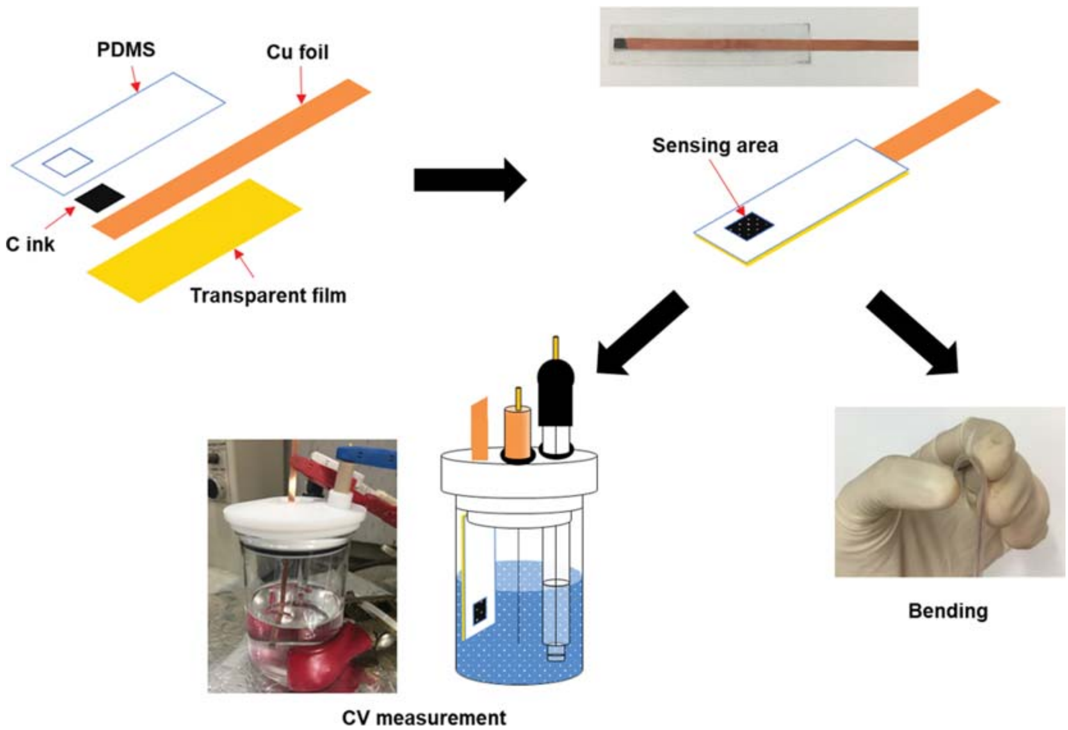

Fig. S12. Schematic illustration of the fabrication process of flexible NC(1) sensor.

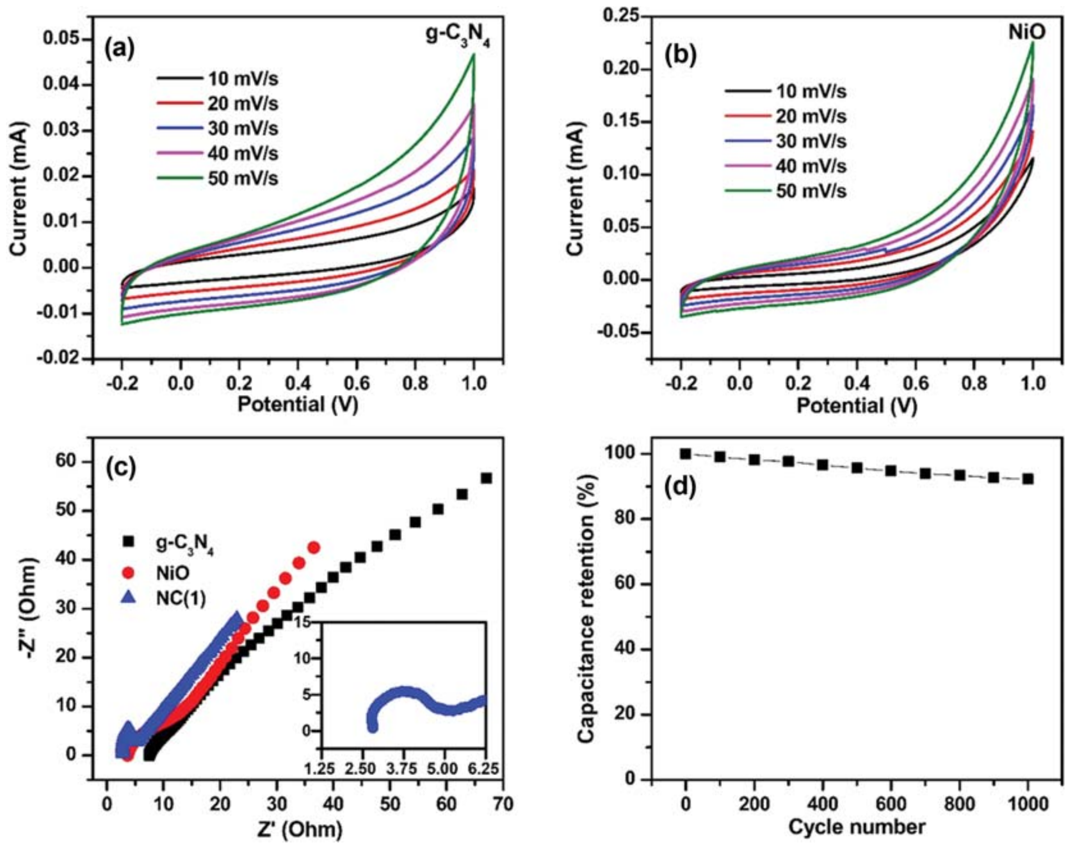

Fig. S13. (a)-(b) CV curves of g-C_3N_4 and NiO at different scan rates. (c) Nyquist plots of g-C_3N_4, NiO and NC(1) with the frequency range from 0.01 Hz to 1,000 kHz, where Z′ is real impedance and Z″ is imaginary impedance. (d) Cycle performance measured at 1 A g^{-1} for 1,000 cycles. The inset (d) is equivalent circuit.

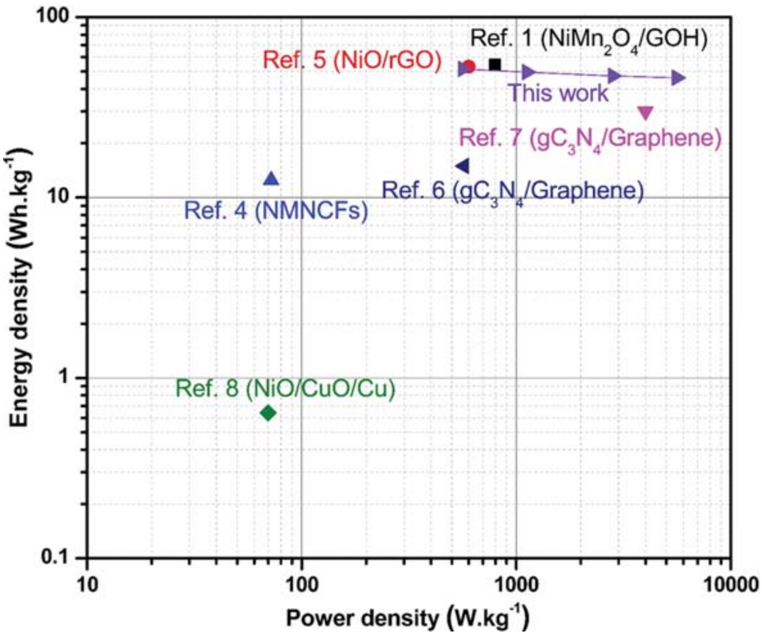

Fig. S14. Ragone plots of various previous studies along with that of NiO/g-C_3N_4 in this study [1,4-8].

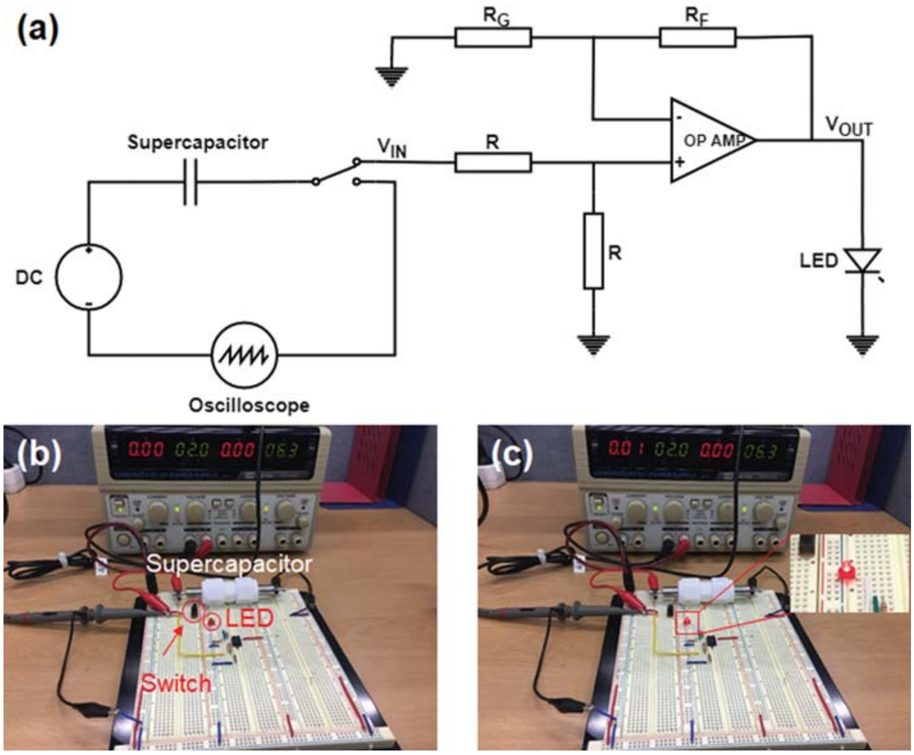

Fig. S15. Circuit diagram (a) and optical images of a LED (b) before and (c) after powered by NC(1) supercapacitor connected in a series.

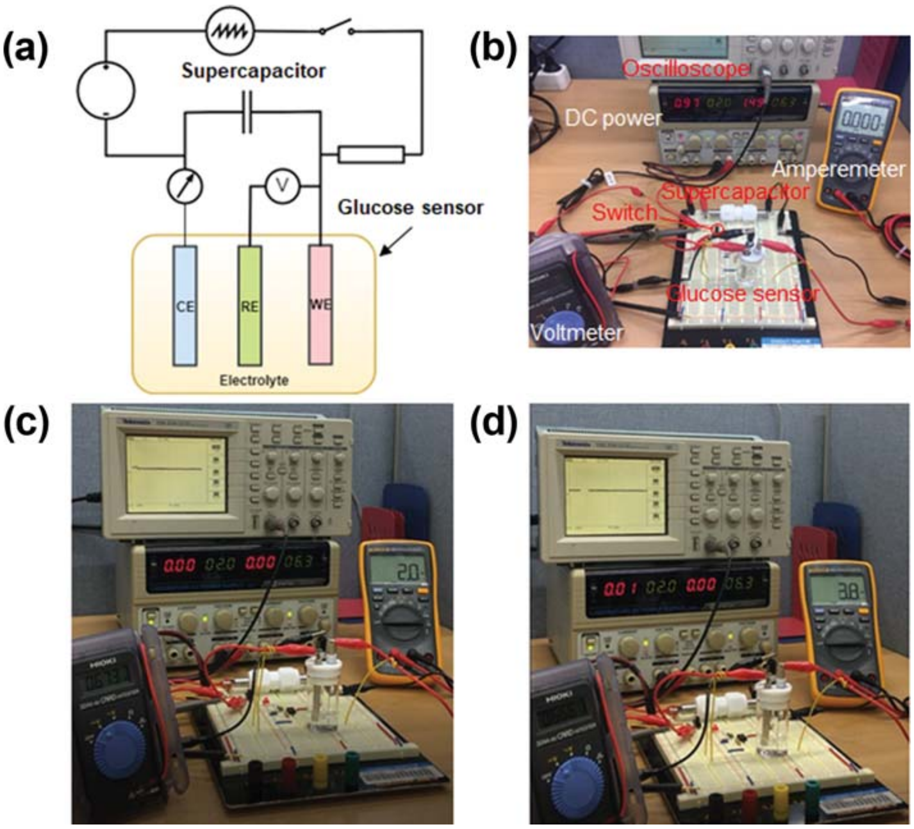

Fig. S16. (a) Circuit diagram and (b) digital photographs of the test circuit of NC(1) based self-powered glucose sensing system. The current measurement using the amperemeter (c) before and (d) after adding 1 mM glucose.

Table S3. The BET surface area and glucose sensitivity of various samples fabricated in this study

Samples	Ratio of $Ni(OH)_2$: Melamine	S_{BET} (m^2/g)	Pore size (nm)	Sensitivity ($\mu A \cdot mM^{-1} \cdot cm^{-2}$)	Correlation coefficient (R^2)
$g\text{-}C_3N_4$	0 : 1	14.50	16.71	194.01*	0.9168
NiO	1 : 0	39.52	10.55	974.31	0.9838
NC(0.5)	1 : 0.5	48.13	8.31	3,881.9	0.9884
NC(1)	1 : 1	54.74	6.80	5,387.1	0.9929
NC(2)	1 : 2	30.92	8.18	3,403.6	0.9792
NC(3)	1 : 3	23.92	10.94	2,742.3	0.9784
NC(4)	1 : 4	19.93	11.32	1,140.0	0.9850

*The sensitivity of $g\text{-}C_3N_4$ was obtained by CV curves at +0.8 V with the change of current as increasing glucose concentration. Other samples were obtained at the oxidation peak of Ni^{2+}/Ni^{3+} at +0.68 V.

Table S4. Performance comparison of NiO/$g\text{-}C_3N_4$ based electrode and other non-enzymatic glucose sensor

Material electrode	Linear range	Sensitivity ($mA \cdot mM^{-1} cm^{-2}$)	Low detection limit (LOD)	Response time (s)	Ref.
Hedgehog-NiO	0.1-5 mM	1,052.8	1.2 μM	-	[9]
NiO@Ag NWs	0-1.28 mM	67.51	1.01 μM	7	[10]
NiO/rGO	3.13 μM-3.05 mM	1,087	1 μM	~10	[11]
NiO/CuO/PANI	20-2,500 μM		2 μM	5	[12]
Ag/NiO/rGO	50 μM-7.5 mM 10-25 mM	1,869.4 115.8	2.44 μM 1.22 mM	<4	[13]
$g\text{-}C_3N_4$-GOD*	1-12 mM	-	11 mM	-	[14]
$Cu^{2+}\text{-}C_3N_4$/MWCNT	0.5 μM-12 mM	929	0.35 μM	<3	[15]
AgNPs-CNx**	0.001-0.1 mM	97	0.6 μM	-	[16]
NiO/$g\text{-}C_3N_4$	500 nM-0.1 mM 0.1-20 mM	5,387.1 49.06	2.30 μM 1.13 mM	<4	This study

* GOD - glucose oxidase, ** CN_x - graphitic carbon nitride

REFERENCES

1. Y.-L. T. Ngo, L. Sui, W. Ahn, J. S. Chung and S. H. Hur, *Nanoscale*, **9**, 19318 (2017).
2. A. Roy, A. Ray, S. Saha, M. Ghosh, T. Das, B. Satpati, M. Nandi and S. Das, *Electrochim. Acta*, **283**, 327 (2018).
3. Z. S. Wu, K. Parvez, X. Feng and K. Müllen, *Nat. Commun.*, **4**, 2487 (2013).
4. Q. Liang, L. Ye, Q. Xu, Z.-H. Huang, F. Kang and Q.-H. Yang, *Carbon*, **94**, 342 (2015).
5. W. Li, Y. Bu, H. Jin, J. Wang, W. Zhang, S. Wang and J. Wang, *Energy Fuels*, **27**, 6304 (2013).
6. R. Lin, Z. Li, D. I. AbouElAmaiem, B. Zhang, D. J. L. Brett, G. He and I. P. Parkin, *J. Mater. Chem. A*, **5**, 25545 (2017).
7. Q. Chen, Y. Zhao, X. Huang, N. Chen and L. Qu, *J. Mater. Chem. A*, **3**, 6761 (2015).
8. A. Al-Osta, B. S. Samer, V. V. Jadhav, U. T. Nakate, R. S. Mane and M. Naushad, *J. Solid. State. Electrochem.*, **21**, 2609 (2017).
9. R. A. Soomro, Z. H. Ibupoto, Sirajuddin, M. I. Abro and M. Willander, *Sens. Actuators, B: Chem.*, **209**, 966 (2015).
10. J. Song, L. Xu, R. Xing, W. Qin, Q. Dai and H. Song, *Sens. Actuators, B: Chem.*, **182**, 675 (2013).
11. B. Yuan, C. Xu, D. Deng, Y. Xing, L. Liu, H. Pang and D. Zhang, *Electrochim. Acta*, **88**, 708 (2013).
12. K. Ghanbari and Z. Babaei, *Anal. Biochem.*, **498**, 37 (2016).
13. Y.-L. T. Ngo, L. T. Hoa, J. S. Chung and S. H. Hur, *J. Alloys Compd.*, **712**, 742 (2017).
14. J. Tian, Q. Liu, C. Ge, Z. Xing, A. M. Asiri, A. O. Al-Youbi and X. Sun, *Nanoscale*, **5**, 8921 (2013).
15. W. Zheng, Y. Li, M. Liu, C.-S. Tsang, L. Y. S. Lee and K.-Y. Wong, *Electroanalysis*, **30**, 1446 (2018).
16. M. K. Kundu, M. Sadhukhan and S. Barman, *J. Mater. Chem. B*, **3**, 1289 (2015).